Antarct. Meteorite Res., **10**, 227–248, 1997

TITANIUM-RICH OXIDE-BEARING PLAGIOCLASE-OLIVINE INCLUSIONS IN THE UNUSUAL NINGQIANG CARBONACEOUS CHONDRITE

Yangting LIN[1,2] and Makoto KIMURA[1]

[1]*Department of Earth Sciences, Ibaraki University, Mito 310*
[2]*Guangzhou Institute of Geochemistry, Chinese Academy of Sciences, Guangzhou 510640, China*

Abstract: Two plagioclase-olivine inclusions (POIs) from the unusual Ningqiang carbonaceous chondrite were studied to understand their mineralogy and crystallization history. In addition to the major phases plagioclase, spinel, olivine and pyroxene, Ningqiang POIs are characterized by interstitial assemblages composed of Ca-rich and Ca-poor pyroxenes, Ti-rich oxides and the other phases. The Ti-rich oxides include an unidentified titanium mineral series referred to as phase T, Ca-rich and Mg, Fe-rich armalcolites, geikielite, perovskite and rutile. This is the first reported occurrence of Ca-rich armalcolite and geikielite, and the second report of phase T in meteorites. Most of the constituent phases crystallized from the POI melts, and the Ti-rich oxides were the last phases in the crystallization sequence. Precipitation of the Ti-rich oxides may be related to the low abundance of Ca-rich pyroxene in the POIs.

1. Introduction

Plagioclase-olivine inclusions (hereafter POIs) are characteristic inclusions in carbonaceous chondrites, and mainly consists of plagioclase, olivine, pyroxene and spinel. However, in comparison with the other types of refractory inclusions, there are only few reported studies of POIs. SHENG *et al.* (1991) demonstrated that POIs are distinguished in mineralogy, chemistry and isotopic compositions from the other types of inclusions and Al-rich chondrules. They probably represent intermediate assemblages between more refractory inclusions and chondrules. Several rare phases, such as armalcolite (HAGGERTY, 1978; SHENG *et al.*, 1991) and an unidentified titanium mineral series ($R^{2+}R^{4+}{}_3O_7-R^{3+}{}_2R^{4+}{}_2O_7$) referred to as phase T (HAGGERTY, 1978), were found in POIs.

The Ningqiang meteorite was first classified as an anomalous CV3 (RUBIN *et al.*, 1988) and later reclassified as an anomalous CK3 (KALLEMEYN *et al.*, 1991). Recently, KALLEMEYN (1996) suggested that it does not fit into any known chondrite group. However, it shares many petrologic and oxygen isotopic characteristics with the oxidized CV3 chondrites, and it may be related to that group (WEISBERG *et al.*, 1996; KIMURA *et al.*, 1997). In the Ningqiang meteorite, only a few refractory inclusions have been reported, and its abundance was estimated to be $1.0^{+1.0}_{-0.5}$ vol% (RUBIN *et al.*, 1988). During a systematic study of this meteorite, we found 124 refractory inclusions

from 21 thin sections (a total surface of 17.4 cm^2), suggestive of an abundance of 2.5 vol% (LIN *et al.*, 1996). Of the inclusions, Type A (melilite-rich) are the most abundant, and the most are fluffy aggregates. Spinel-pyroxene-inclusions are second in abundance. Other less abundant inclusions are a new kind of anorthite-spinel-rich inclusions (LIN and KIMURA, 1996a) and Type B (pyroxene-melilite-spinel-rich). Additionary, there are a single Type C (plagioclase-pyroxene-rich) and one POI (plagioclase-olivine-rich) inclusion. The latter is one of the POIs reported in this paper. The other one was previously described by RUBIN *et al.* (1988) as consisting of plagioclase, spinel and olivine, and it is reexamined in this work. In addition to plagioclase, olivine and spinel, in this inclusion, we found complicated assemblages consisting of Ca-rich and Ca-poor pyroxenes, wollastonite, chromite and varieties of Ti-rich oxides such as phase T, (Mg, Fe)-armalcolite, Ca-armalcolite, geikielite, rutile and perovskite. This is the first report of Ca-armalcolite and geikielite, and second report of phase T in a meteorite. Based on a detailed petrographical and mineralogical study, the formation of the POIs and their Ti-rich oxides are discussed. The preliminary work was reported by LIN and KIMURA (1996b).

2. Samples and Experimental Methods

The POI found during this study is labeled as *W2#4*, and the other one previously described by RUBIN *et al.* (1988) is labeled as *C#1* hereafter.

Both of the POIs were studied using an optical microscope and a JEOL 733 electron microprobe. Quantitative analyses for silicates were carried out with a 15 kV accelerating voltage and a 20 nA beam current. The Ti-rich oxides were analyzed with a 20 kV accelerating voltage. An X-ray peak deconvolution program was applied to correct for X-ray overlaps of the K_α lines by K_β lines of some successive elements (*e.g.*, V overlapped by Ti and Mn by Cr) and L_α line of Zr by K_α line of Sc. Overlapping of Ca line to Sc (EL GORESY *et al.*, 1984) was below detection in this work. Analytical results of the Ti-rich oxides were corrected by ZAF method and the others were corrected by Bence-Albee method (BENCE and ALBEE, 1968). Modal compositions of the inclusions were calculated on the basis of phase areas on the back scatter electron (BSE) images. The bulk compositions of *W2#4* and *C#1* were calculated from their modal and average compositions of the constituent phases. In order to check the accuracy of the calculated bulk compositions, the bulk composition of *W2#4* was also measured using the defocused beam (50 μm in diameter) rastering the whole inclusion.

3. Petrography

Inclusion *W2#4* (>2.0 mm) has a spherical shape, although some parts of it have been lost during thin section preparation. This inclusion has two texturally distinct parts. One part of it (~3/5 of the whole inclusion) consists mainly of dendritic plagioclase (20–40 μm in width, up to 600 μm in length) enclosing numerous fine-grained Ca-poor pyroxene grains (<10 μm in width) (Fig. 1a, b). Interstitial to the plagioclase, are fine-grained assemblages, hereafter interstitial assemblage, consisting of Ca-rich pyroxene, plagioclase, Ti-rich oxides and unidentified fine-grained mixtures. Ca-rich

Fig. 1a. A low magnification back scatter electron (BSE) image of the dendritic part of W2#4, showing plagioclase with numerous Ca-poor pyroxene inclusions. The width is 490 μm.

Fig. 1b. A magnified area of (a), showing orientation of the Ca-poor pyroxene (Px) in plagioclase (Pl) and occurrence of Ca-rich pyroxene (CPx) along boundary of the interstitial assemblages. Fine and bright grains in the interstitial assemblages are Ti-rich oxides (indicated by arrows). The width is 190 μm.

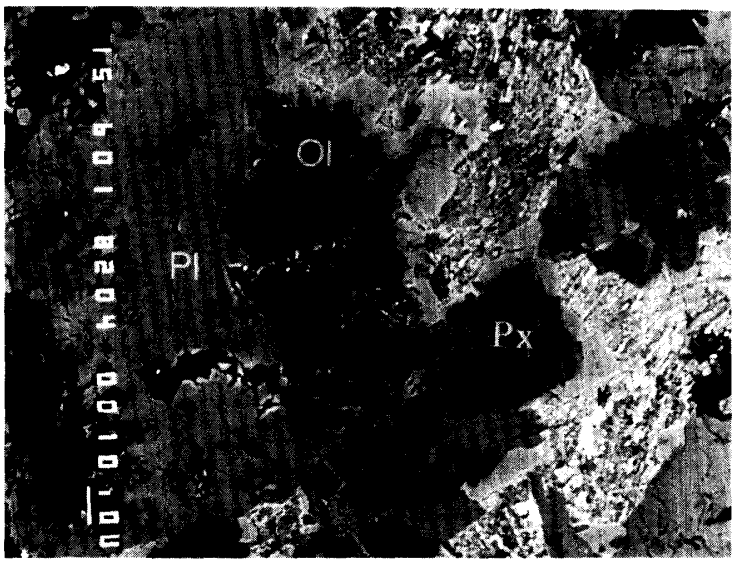

Fig. 1c. The interstitial assemblage in the poikilitic part of W2#4. Ca-rich pyroxene surrounds plagioclase and Ca-poor pyroxene and olivine (Ol). Fine and bright grains in the interstitial assemblages are Ti-rich oxides. Dark areas are voids due to thin section preparation. The width is 190 μm.

pyroxene mainly occurs along the boundary of the interstitial assemblages (Fig. 1b). The other part of the inclusion shows poikilitic texture, consisting of euhedral to subhedral plagioclase (<50 μm in width) and Ca-poor pyroxene (<60 μm in size) with a few olivine grains (<70 μm in size). The interstitial assemblages are also encountered among plagioclase and Ca-poor pyroxene in this part of the inclusion, with Ca-rich pyroxene mantling the Ca-poor pyroxene along the boundary of the interstitial assemblages (Fig. 1c). Both textural parts seem to be continuous in texture, and have nearly similar modal compositions, except for the occurrences of olivine and a few round spinel crystals (<10 μm in size) enclosed in plagioclase in the poikilitic part. The modal composition of the whole inclusion is: 53 vol% plagioclase, 30 vol% Ca-poor pyroxene, 15 vol% Ca-rich pyroxene, 2 vol% olivine with minor Ti-rich oxides and

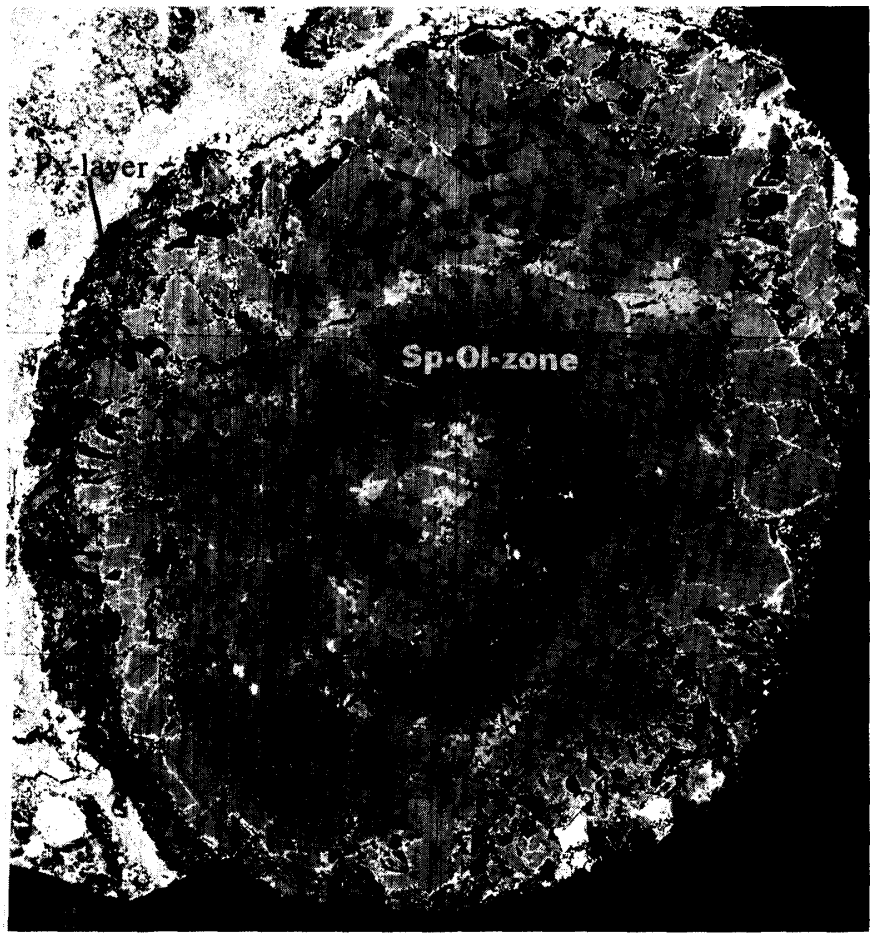

Fig. 2a. Photomosaic of back scatter electron image of C#1, which consists mainly of euhedral and coarse-grained plagioclase. In the central area of the inclusion, there is a zone (Sp-Ol-zone) composed of abundant fine-grained inclusions of spinel and olivine (not labeled here) in plagioclase. In the marginal area, olivine is coarse-grained and occurs associated with or enclosed within plagioclase. Note that many bright interstitial assemblages occur with plagioclase and/or olivine. Also evident is a pyroxene layer (Px-layer) partially surrounding the inclusion. The long axis of the inclusion is 3.0 mm.

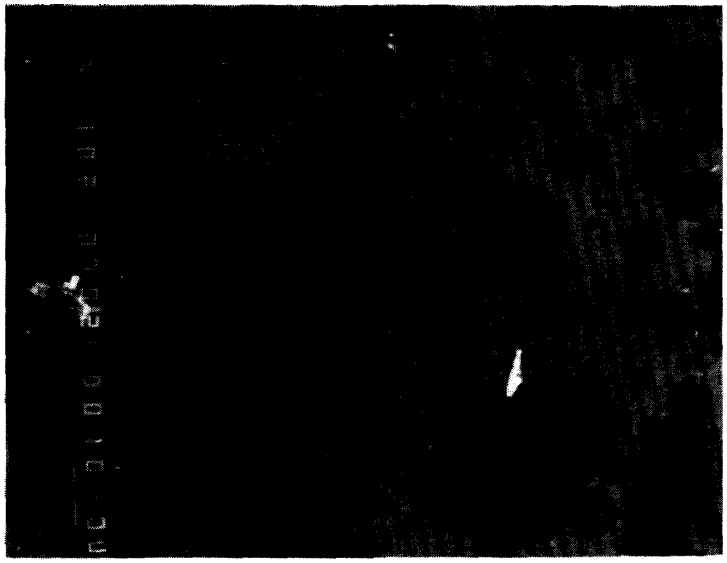

Fig. 2b. High magnification image of the spinel-olivine-rich zone, showing thin bright-rim of spinel (Sp) due to Cr_2O_3-enrichment. On the right of the photo, there are some brighter spinels also enriched in Cr_2O_3. Olivine in this zone is fine-grained. The width is 110 μm.

Fig. 2c. High magnification image of the marginal area near the spinel-olivine-rich zone (left of the photo), showing the coarse-grained and euhedral to subhedral olivine in and among plagioclase. The assemblage, composed of Ca-rich pyroxene, Ca-poor pyroxene and Ti-rich oxides (bright grains), is interstitial to plagioclase and olivine. The width is 360 μm. The other abbreviations are the same as above.

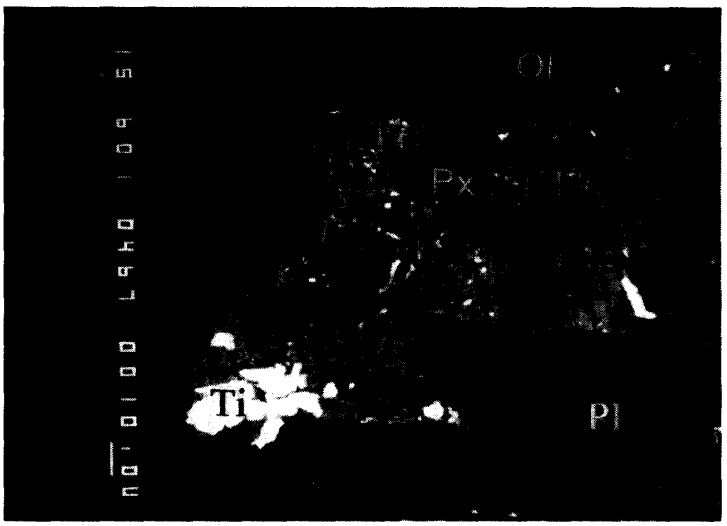

Fig. 3. An interstitial assemblage in C#1, consisting of Ca-rich and Ca-poor pyroxenes, Ti-rich oxides (Ti) and unidentified fine-grained mixture. The width is 260 μm.

the unidentified fine-grained mixtures.

Inclusion *C#1* (2.5×3.0 mm) was reported to contain 71 vol% plagioclase, 25 vol% spinel and 4 vol% olivine based on modal point counting (171 points) (RUBIN *et al.*, 1988). However, our calculated modal composition is significantly different, with 59 vol% plagioclase, 14 vol% spinel, 14 vol% olivine, 7 vol% Ca-rich pyroxene, 5 vol% Ca-poor pyroxene, 1 vol% Ti-rich oxides and the other accessory phases. These differences may partially be due to the different methods used. In the case of modal point counting under optical microscope, it was hardly to recognize fine-grained olivine associated with abundant spinel in the center of the inclusion. Another reason is that pyroxene was neglected in Rubin's modal composition. In *C#1*, plagioclase is euhedral and coarse-grained (up to 380 μm in size) (Fig. 2a). Spinel (euhedral and <20 μm in size) occurs as inclusions in plagioclase and olivine in the whole inclusion but predominantly in the central area, labeled as spinel-olivine-rich zone in Fig. 2a. The spinel in this zone usually has a thin rim that appears bright in BSE. Additionary, some spinel grains appear brighter than the others in BSE image (Fig. 2b). The bright grains are enriched in Cr_2O_3 (Table 3), and analyses close to the bright rim also show Cr_2O_3-enrichment, similar to spinels in the POIs from CV3s (SHENG *et al.*, 1991). Olivine shows two types of occurrences. Most of the olivine is coarse-grained (50–240 μm in size) and subhedral to euhedral in form. It occurs associated or enclosed within plagioclase in the marginal area of the inclusion (Fig. 2a and c). The rest is fine-grained (<35 μm) and anhedral to subhedral in form, and is associated with abundant spinel in the spinel-olivine-rich zone of the inclusion (Fig. 2b). We observed that olivines enclosed in single crystals of plagioclase in this zone show extinction in the same direction.

C#1 is also characterized by the occurrence of interstitial assemblages associated with plagioclase and olivine (Figs. 2, 3), which consist of Ca-rich and Ca-poor pyroxenes and Ti-rich oxides with minor wollastonite, awaruite, chromite and unidentified fine-grained mixtures. However, the Ti-rich oxides are much more abundant and coarser (≤35 μm) than those in *W2#4*. Phase T is the most abundant among the Ti-rich oxides. In the BSE image, phase T appears to be heterogeneous (Fig. 4a), reflecting variation in its Ca, Mg and Fe contents (Table 6). Ca-rich armalcolite is the second most abundant Ti-rich oxide and it coexists with phase T. Figure 4b shows an intergrowth of Ca-rich armalcolite with phase T and geikielite. Only one grain of the Ti-rich oxide contains both Ca-rich armalcolite and perovskite. Two tiny grains of rutile enclosed in phase T in another Ti-oxide assemblage were found.

The other characteristic feature of *C#1* is the presence of a pyroxene layer (100–150 μm in width), partially surrounding host of the inclusion (Fig. 2a). The pyroxene layer is predominantly composed of Ca-poor and Ca-rich pyroxenes (64 and 36 vol%, respectively) with a few grains of plagioclase (<40 μm). Ca-poor pyroxene is generally mantled by Ca-rich pyroxene, and both of them are in close contact with plagioclase and olivine of the host (Fig. 5). Neither Ti-rich oxides, wollastonite, chromite nor the other phase are found in the pyroxene layer.

The degree of alteration of Ningqiang POIs is as weak as that in the POIs in CV3 chondrites (SHENG *et al.*, 1991). In *C#1*, secondary alteration took place near the interface between the pyroxene layer and the host, forming a thin hedenbergite rim along

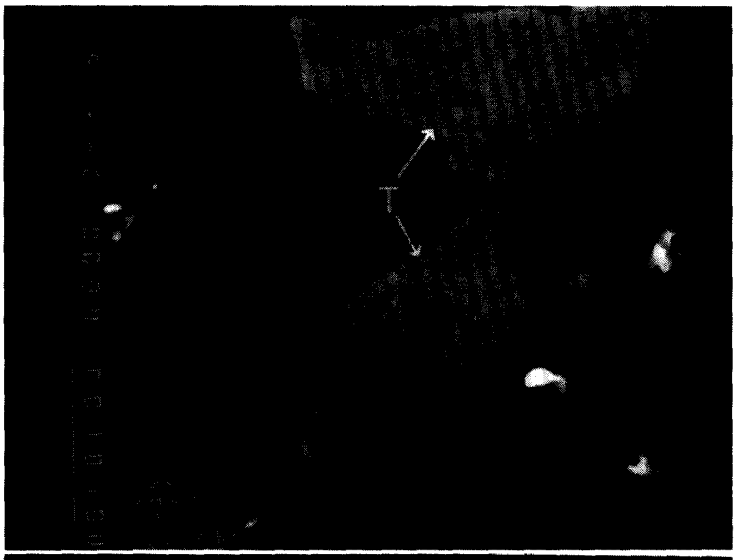

Fig. 4a. BSE image of phase T, showing its heterogeneous composition. The width is 45 μm.

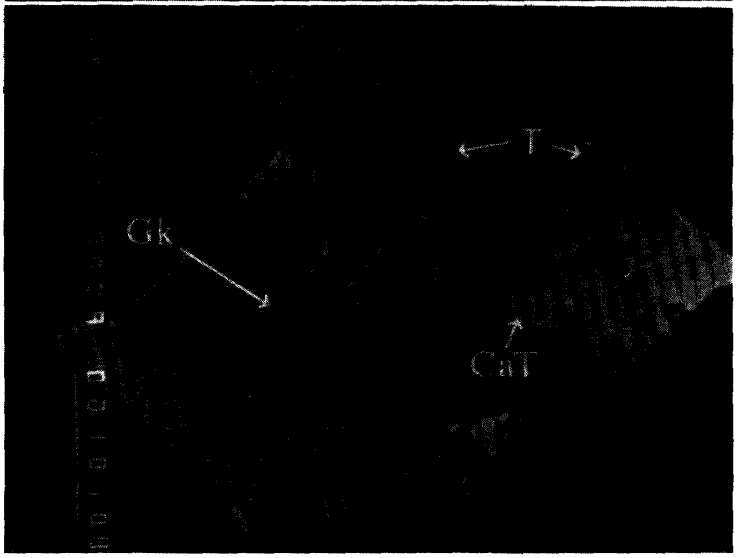

Fig. 4b. A large grain of Ti-rich oxides, consisting of phase T (T), Ca-rich armalcolite (CaT) and geikielite (Gk). Phase T is also heterogeneous. Geikielite is closely associated with Ca-rich armalcolite. The width is 48 μm.

Fig. 5. A part of the pyroxene layer in C#1. Ca-poor pyroxene is usually mantled by Ca-rich pyroxene, and both of them are closely in contact with plagioclase and olivine of the host. The thin bright rims along boundaries and/or cracks of plagioclase and olivine are hedenbergite (Hed). The width is 590 μm.

grain boundaries and/or cracks in plagioclase and olivine (Fig. 5). Some olivines and spinels show normal zoning toward the hedenbergite rim. Alteration features were not found in *W2#4*.

4. Bulk Composition

Table 1 gives the bulk compositions of *W2#4* and *C#1*. The calculated and measured bulk compositions of the *W2#4* are nearly the same. In comparison with the deviation between the two methods, the differences between the bulk compositions of *W2#4* and *C#1* are significant. *C#1* contains higher Al_2O_3 (30.0%), MgO (16.6%) and TiO_2 (2.31%), and lower SiO_2 (37.3%) and Na_2O (0.59%) than *W2#4* (17.6% Al_2O_3, 15.5% MgO, 0.74% TiO_2, 51.2% SiO_2 and 1.08% Na_2O), but their CaO are nearly the same (*C#1*: 12.1% CaO, *W2#4*: 12.7% CaO). The bulk composition of *C#1* is in the range of group I (abundant spinel and plagioclase), and *W2#4* in the range of group II (minor spinel and abundant plagioclase) of the POIs in CV3 chondrites (SHENG *et al.*, 1991).

Table 1. Bulk compositions of Ningqiang POIs (wt%).*

	C#1[§]	*W2#4*[§]	*W2#4*[†]
SiO_2	37.3	51.1	51.2
TiO_2	2.31	0.61	0.74
Al_2O_3	30.0	17.7	17.6
Cr_2O_3	0.76	0.85	0.65
FeO	0.62	1.00	0.45
MnO	0.03	0.22	0.14
MgO	16.6	14.9	15.5
CaO	12.1	12.3	12.7
Na_2O	0.59	1.28	1.08
K_2O	0.00	0.04	0.00

* Normalized to 100%.
[§] Determined by calculation from modal and average compositions of the constituents.
[†] Determined by defocused beam analysis.

5. Mineral Chemistry

Plagioclase: Table 2 gives representative analyses of plagioclase in both inclusions. In *C#1*, many plagioclase laths are normally zoned from $An_{94\text{-}96}$ in the cores to $An_{80\text{-}87}$ in the thin rims (~10 μm in width). The compositions of the cores are nearly the same among grains. Plagioclase in the pyroxene layer is also anorthitic ($An_{82\text{-}93}$). Normal zoning of plagioclase from $An_{88\text{-}84}$ in the cores to $An_{83\text{-}77}$ in the rims is also encountered in the poikilitic part of *W2#4*. Plagioclase in the dendritic part has an An-content (79–85 mol%) similar to that in the poikilitic part. In comparison with *C#1*, the An-content is lower in *W2#4*. Some grains in the interstitial assemblages of *W2#4* are more sodic (An_{68}). The MgO-content (0.20–0.62%) is always low both in

Table 2. Representative compositions of plagioclase (wt%).

	C#1						*W2#4*				
	1§	2†	3§	4†	5§	6†	7§	8†	9	10	11
SiO_2	44.3	46.7	43.9	47.8	45.3	46.7	44.5	45.6	45.7	46.5	58.0
TiO_2	0.06	0.11	0.10	0.16	0.06	n.d.	n.d.	n.d.	n.d.	n.d.	0.30
Al_2O_3	34.4	32.5	34.7	31.5	32.8	32.4	33.7	32.6	33.1	33.2	19.8
FeO	0.04	0.23	n.d.	0.15	0.78	1.22	0.04	0.08	0.75	n.d.	0.17
MgO	0.50	0.35	0.34	0.50	0.43	0.25	0.41	0.56	0.21	0.20	0.33
CaO	19.8	18.2	20.0	17.3	18.4	17.8	17.9	17.2	17.4	16.6	17.0
Na_2O	0.73	1.88	0.76	2.22	1.56	1.97	1.51	1.97	1.73	2.45	4.45
K_2O	n.d.	n.d.	n.d.	n.d.	n.d.	n.d.	n.d.	n.d.	n.d.	n.d.	n.d.
Total	99.8	99.9	99.7	99.6	99.3	100.3	98.0	98.0	98.9	98.9	100.1
	normalized to oxygen number of 8										
Si	2.056	2.159	2.044	2.210	2.116	2.160	2.095	2.144	2.135	2.162	2.656
Ti	0.002	0.004	0.003	0.005	0.002	0.000	0.000	0.000	0.000	0.000	0.010
Al	1.885	1.771	1.902	1.715	1.803	1.764	1.869	1.806	1.823	1.817	1.069
Fe	0.001	0.009	0.000	0.006	0.031	0.047	0.002	0.003	0.029	0.000	0.006
Mg	0.034	0.024	0.024	0.035	0.030	0.017	0.029	0.039	0.015	0.014	0.022
Ca	0.988	0.900	0.995	0.856	0.918	0.881	0.904	0.870	0.873	0.825	0.836
Na	0.065	0.169	0.068	0.199	0.141	0.176	0.138	0.180	0.157	0.221	0.395
K	0.000	0.000	0.000	0.000	0.000	0.000	0.000	0.000	0.000	0.000	0.000
Sum	5.031	5.036	5.036	5.026	5.041	5.045	5.037	5.042	5.033	5.040	4.996
An	93.8	84.2	93.6	81.1	86.7	83.3	86.8	82.9	84.8	78.9	67.9

Note: 1) Occurrences of plagioclases in the host (1–4), pyroxene layer (5–6), poikilitic part (7–8), dendritic part (9–10) and interstitial assemblage (11).
2) §: core of plagioclase; †: rim of plagioclase.
3) n.d. - below detection limits, which are 0.01 for MgO, CaO, Na_2O and K_2O, 0.02 for TiO_2, Al_2O_3 and Cr_2O_3, 0.03 for FeO and MnO, and 0.04 for SiO_2 (1σ).

C#1 and *W2#4*, and not related with the Na_2O-content as reported in the POIs in CV3 chondrites (SHENG *et al.*, 1991).

Spinel: Table 3 gives representative compositions of the spinel. In *C#1*, the bright grains of spinel in the spinel-olivine-rich zone are characterized by high contents of Cr_2O_3 and TiO_2 (up to 15.2% and 2.8%, respectively), while the spinels in the other textural settings are lower in these components (0.52–1.65% and 0.20–0.65%, respectively). Although the bright rim of the spinel is too thin to analyze, analyses close to the rim show increase in Cr_2O_3-content. The V_2O_3-content is also higher in the bright spinel grains (up to 0.88%) than that in the other grains (0.18–0.28%). In *W2#4*, the TiO_2-content of spinel is distinctly lower (0.16–0.20%), while the contents of Cr_2O_3 (1.98–4.29%) and V_2O_3 (0.31–0.38%) fall in the ranges of *C#1*. Figure 6a shows a positive relationship between the Cr_2O_3 and V_2O_3 contents in the Ningqiang POIs. Most of spinels in both *W2#4* and *C#1* have low FeO-content (0.36–1.68%), except the grains near the hedenbergite-rim (up to 11% FeO) (Fig. 6b).

Olivine: Most of the olivine in *C#1* and all in *W2#4* are close to pure forsterite ($Fo_{>99}$). The FeO-bearing grains (Fa_{2-6}) occur near the hedenbergite-rim in *C#1*. Olivines contain minor CaO (0.08-0.30%), Cr_2O_3 (<0.24%) and MnO (<0.16%).

Table 3. Representative compositions of spinel (wt%).

	C#1								*W2#4*		
	1	2	3	4	5	6	7	8	9	10	11
SiO_2	n.d.	n.d	n.d.	n.d.	0.33	n.d.	n.d.	n.d.	0.54	0.27	0.12
TiO_2	0.44	0.23	0.75	1.16	2.49	0.27	0.36	0.30	0.18	0.18	0.20
Al_2O_3	71.4	70.8	69.5	62.8	54.2	70.3	68.1	68.0	66.7	69.6	66.8
Cr_2O_3	0.52	1.20	1.68	5.67	14.63	0.67	1.63	1.40	4.29	1.98	3.65
V_2O_3	0.23	0.21	0.27	0.41	0.90	0.21	0.17	0.23	0.36	0.31	0.36
FeO	1.02	0.86	0.48	1.67	1.88	2.37	7.77	8.26	1.47	0.49	0.48
MnO	n.d.	n.d.	0.03	n.d.	0.06	n.d.	n.d.	n.d.	n.d.	n.d.	n.d.
MgO	27.7	28.0	28.1	26.5	25.72	26.8	23.0	22.2	27.1	27.4	27.3
CaO	0.04	0.04	0.04	0.09	0.23	0.18	0.05	0.08	0.12	0.10	0.04
ZnO	n.d.	n.d.	n.d.	n.d.	n.d.	n.d.	0.23	0.30	n.d.	n.d.	n.d.
Na_2O	n.d.	n.d.	n.d.	n.d.	n.d.	n.d.	n.d.	n.d.	n.d.	n.d.	n.d.
Total	101.3	101.4	100.9	98.3	100.5	100.9	101.3	100.8	100.8	100.3	99.1
	normalized to oxygen number of 4										
Si	0.000	0.000	0.000	0.000	0.009	0.000	0.000	0.000	0.013	0.007	0.003
Ti	0.008	0.004	0.014	0.022	0.047	0.005	0.007	0.006	0.003	0.004	0.004
Al	1.981	1.967	1.943	1.838	1.609	1.974	1.958	1.967	1.888	1.954	1.913
Cr	0.010	0.023	0.032	0.112	0.291	0.013	0.032	0.027	0.082	0.038	0.070
V	0.005	0.004	0.005	0.008	0.018	0.004	0.004	0.005	0.007	0.006	0.007
Fe	0.020	0.017	0.010	0.035	0.040	0.047	0.159	0.170	0.030	0.010	0.010
Mn	0.000	0.000	0.001	0.000	0.002	0.000	0.000	0.000	0.000	0.000	0.000
Mg	0.971	0.985	0.994	0.981	0.966	0.952	0.835	0.814	0.970	0.972	0.990
Ca	0.001	0.001	0.001	0.003	0.006	0.005	0.002	0.002	0.003	0.003	0.001
Zn	0.000	0.000	0.000	0.000	0.000	0.000	0.004	0.006	0.000	0.000	0.000
Na	0.000	0.000	0.000	0.000	0.000	0.000	0.000	0.000	0.000	0.000	0.000
Sum	2.994	3.000	2.998	2.997	2.986	2.999	2.998	2.995	2.995	2.992	2.997

Note: 1) 1–2: isolated in plagioclase; 3–5: in spinel-olivine-rich zone; 6–8: near hedenbergite-rim; 9–11: enclosed in plagioclase.

2) n.d.- below detection limits, which are 0.01 for V_2O_3, 0.04 for NiO, 0.06 for ZnO, and 0.03 for P_2O_5, and the others are the same as above (1σ).

Ca-rich pyroxene: Table 4 shows representative compositions of Ca-rich pyroxenes in the POIs, which are significantly distinguished from those in the other types of refractory inclusions. They are enriched in the enstatite component ($En_{47-63}Wo_{25-38}Fs_{<2}TPx_{3-27}CaTs_{<6}$). Although the contents of Al_2O_3 (2.57–8.56%) and TiO_2 (1.16–9.09%) are in the range of Type C inclusions (WARK, 1987), Ca-rich pyroxenes in the POIs are characterized by high weight ratio of TiO_2/Al_2O_3 (~1:1), consistent with analyses in the POIs in CV3 chondrites (SHENG *et al.*, 1991). Furthermore, calculations based on the assumption of stoichiometry suggest a high ratio of $Ti^{3+}/\sum Ti$ (0.9–1.0). Only some grains in the pyroxene layer may have a lower ratio (0.4–0.7). In addition, Ca-rich pyroxenes in the POIs are Cr_2O_3-bearing (up to 3.35%). Figure 7 demonstrates a relationship between Ca-rich pyroxene composition and occurrence, and a positive relationship between Cr_2O_3 and TiO_2 content. In *C#1*, the contents of Al_2O_3, TiO_2 and Cr_2O_3 are higher in the host (3.35–8.56, 2.35–9.09, and 0.65–1.88%, respectively) than those in the pyroxene layer (2.94–4.12, 1.85–3.29, and 0.58–0.91%,

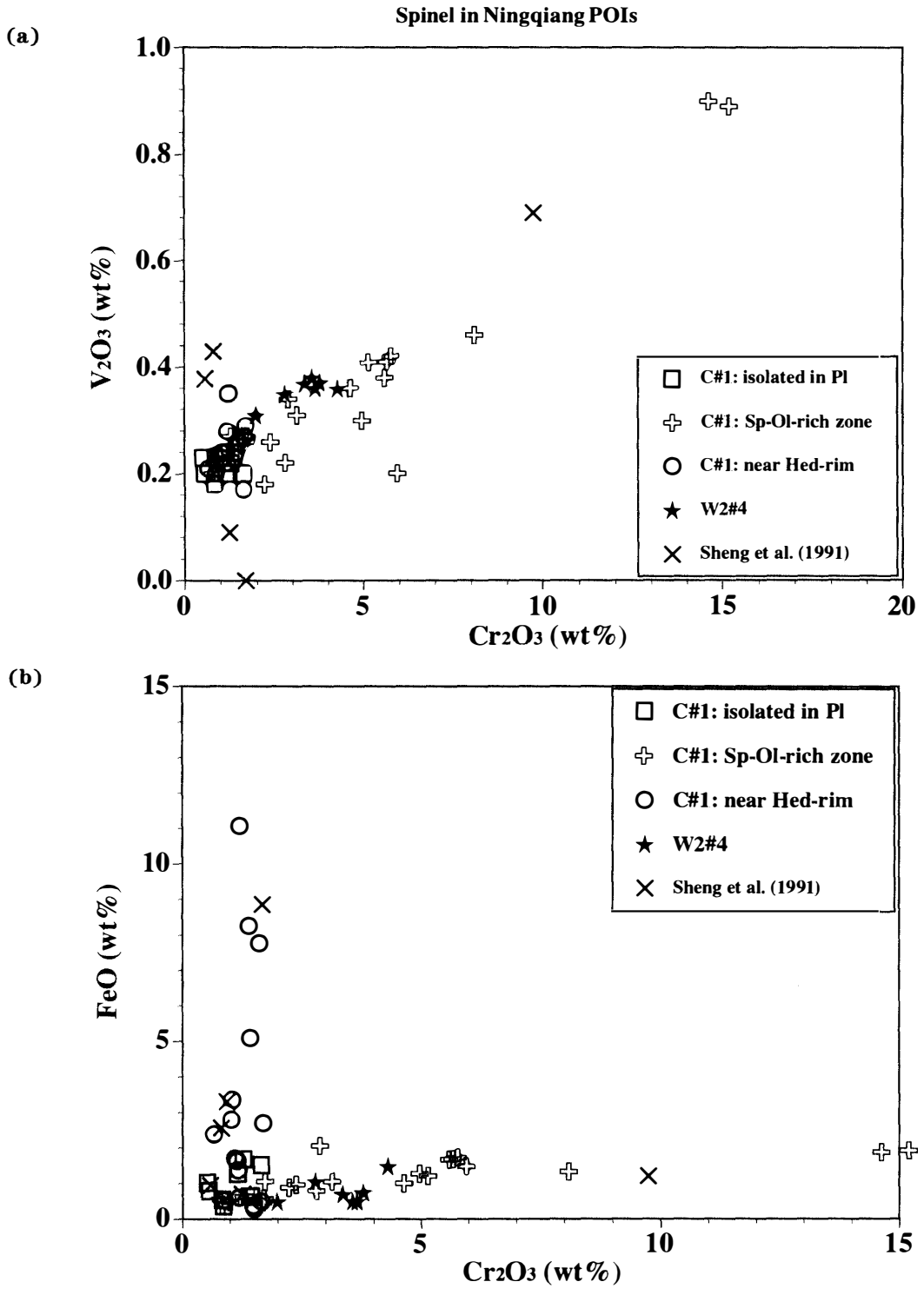

Fig. 6. *(a) Plot of Cr_2O_3 versus V_2O_3, showing a positive relationship between them in Ningqiang POIs. Furthermore, spinel in C#1 shows relationship between the composition and occurrence, with Cr_2O_3 and V_2O_3-rich grains occurring in the spinel-olivine-rich zone, while other grains isolated in plagioclase are lower in these components. (b) Plot of Cr_2O_3 versus FeO, showing FeO-enrichment in spinel grains near hedenbergite rim in C#1. Data reported by* SHENG *et al. (1991) are plotted for comparison. Abbreviations: plagioclase (Pl), spinel (Sp), olivine (Ol) and hedenbergite (Hed).*

Table 4. Representative compositions of Ca-rich pyroxene (wt%).

	W2#4				*C#1*							
	1	2	3	4	5	6	7	8	9	10	11	12
SiO_2	53.5	52.5	50.8	46.1	51.1	48.7	48.0	47.4	52.7	52.2	52.0	51.7
TiO_2	1.60	2.68	3.24	7.55	3.35	5.47	6.73	7.08	2.04	2.53	3.19	3.29
Al_2O_3	3.57	3.36	4.97	7.14	4.38	5.42	5.33	5.42	3.54	3.60	3.36	3.46
Cr_2O_3	0.88	1.13	1.86	3.13	0.84	0.86	1.48	1.18	0.84	0.67	0.82	0.89
V_2O_3	n.d.	n.d.	n.d.	n.d.	n.d.	n.d.	n.d.	n.d.				
FeO	0.41	0.53	0.71	1.31	1.03	0.21	0.42	0.35	0.53	0.27	0.41	0.43
MnO	0.21	0.19	0.37	0.54	0.15	0.10	0.07	0.07	0.11	0.09	0.24	0.37
MgO	20.4	18.5	17.3	14.1	19.1	18.3	16.5	15.9	21.3	20.1	19.8	19.8
CaO	19.0	20.3	20.4	19.8	19.1	20.0	20.6	21.3	18.8	21.2	20.4	20.1
Na_2O	n.d.	n.d.	n.d.	n.d.	0.24	n.d.	n.d.	n.d.	0.05	n.d.	0.05	n.d.
Total	99.5	99.2	99.6	99.7	99.3	99.0	99.2	98.7	100.0	100.6	100.3	100.0
	normalized to oxygen number of 6											
Si	1.912	1.894	1.836	1.688	1.845	1.770	1.751	1.741	1.879	1.860	1.860	1.855
Ti	0.043	0.073	0.088	0.208	0.091	0.149	0.185	0.196	0.055	0.068	0.086	0.089
Al	0.150	0.143	0.212	0.309	0.186	0.232	0.229	0.234	0.149	0.151	0.142	0.146
Cr	0.025	0.032	0.053	0.091	0.024	0.025	0.043	0.034	0.024	0.019	0.023	0.025
V	0.000	0.000	0.000	0.000	0.000	0.000	0.000	0.000				
Fe	0.012	0.016	0.022	0.040	0.031	0.006	0.013	0.011	0.016	0.008	0.012	0.013
Mn	0.006	0.006	0.011	0.017	0.005	0.003	0.002	0.002	0.003	0.003	0.007	0.011
Mg	1.083	0.996	0.931	0.773	1.029	0.989	0.900	0.872	1.133	1.067	1.057	1.058
Ca	0.726	0.784	0.789	0.778	0.740	0.777	0.806	0.839	0.720	0.810	0.783	0.773
Na	0.000	0.000	0.000	0.000	0.017	0.000	0.000	0.000	0.004	0.000	0.003	0.000
Sum	3.958	3.945	3.943	3.904	3.968	3.952	3.928	3.929	3.982	3.987	3.973	3.971
$Ti^{3+}/\Sigma Ti$	1.00	1.00	1.00	1.00	1.00	0.97	1.00	1.00	0.98	0.59	0.94	0.99
TPx	4	4	4	4	4	4	4	4	4	4	4	4
CaTs	5	4	6	5	5	4	2	2	5	3	3	3
Wo	36	38	38	32	34	33	33	34	35	39	36	35
Fs	1	1	1	2	2	0	1	1	1	0	1	1
En	53	50	46	40	51	48	46	44	55	51	52	52

Note: 1) 1–4: in poikilitic part; 5–8: in the host; 9–12: in pyroxene player.
2) n.d.- below detect limits (the same as before).
3) $Ti^{3+}/\Sigma Ti$: calculated with assumption of the stoichiometry.

respectively). In *W2#4*, Ca-rich pyroxene contains 2.57–7.74% Al_2O_3, 1.16–7.55% TiO_2 and 0.78–3.35% Cr_2O_3, with higher Cr_2O_3/TiO_2 ratio than those of *C#1*. In both of the inclusions, Ca-rich pyroxenes contain MnO (<1.03%), but V_2O_3 is below the detection limit.

Ca-poor pyroxene: In *C#1*, Ca-poor pyroxene ($En_{88-95}Fs_1Wo_{4-11}$) also shows relationship between the composition and occurrence (Fig. 8). The grains in the host contain higher TiO_2 (1.02–3.28%) and Cr_2O_3 (0.80–2.01%) than those in the pyroxene layer (0.78–1.31, 0.69–1.10%, respectively). However, the contents of CaO (2.13–5.67%) and Al_2O_3 (1.03–4.08%) are similar in these two occurrences. In *W2#4*, Ca-poor pyroxene ($En_{87-96}Fs_1Wo_{3-12}$) contains lower TiO_2 (0.29–0.98%) than those in *C#1*, while the contents of CaO (1.38–5.88%), Al_2O_3 (1.75–3.92%) and Cr_2O_3

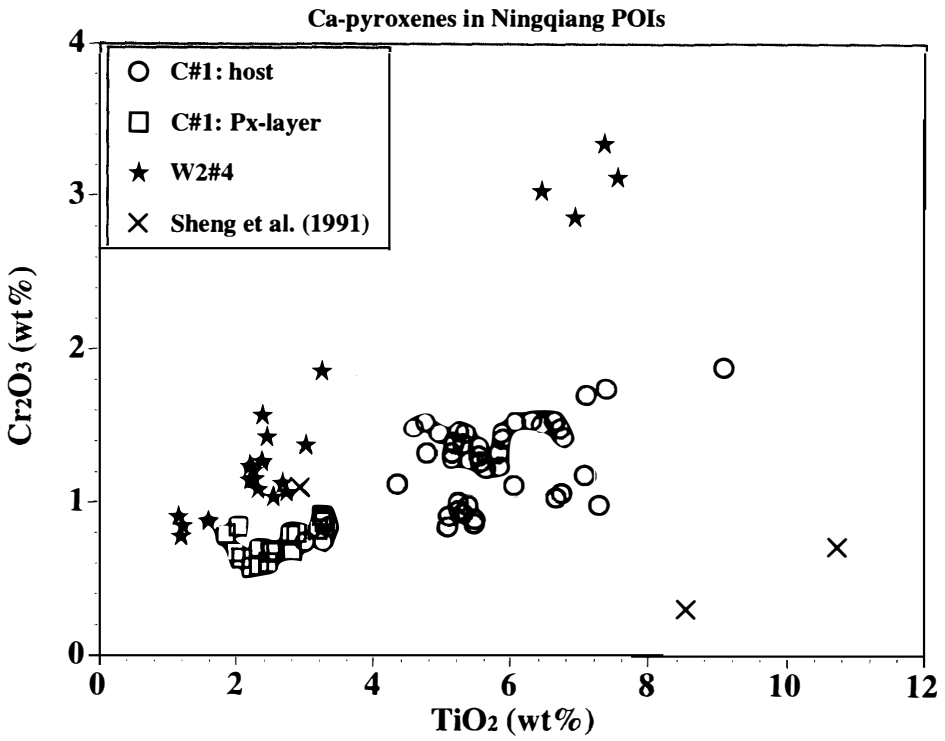

Fig. 7. Plot of TiO_2 versus Cr_2O_3 for Ca-rich pyroxene. The Cr_2O_3-content is positively related with the TiO_2-content in both of the inclusions. In C#1, Ca-rich pyroxenes show relationship between the composition and occurrence. Grains in the host contain higher TiO_2 and Cr_2O_3 than those in the pyroxene layer. In W2#4, Ca-rich pyroxenes show higher ratio of Cr_2O_3/TiO_2.

(0.75–1.62%) fall in the same range as those in *C#1*. In both inclusions, Ca-poor pyroxenes contain minor MnO (<0.43%). Table 5 shows representative analyses of Ca-poor pyroxenes.

Ti-rich oxides: Phase T consists mainly of TiO_2 (77.9–84.0%), CaO (0.62–10.3%), MgO (0.61–11.7%) and FeO (0.34–5.2%). Normalized to an oxygen number of 7, the sum of the cations in phase T is significantly less than 4 (Table. 6), indicative of the presence of Ti^{3+}. Calculation of the Ti^{3+}-content, based on stoichiometry of solid solution of $R^{2+}R^{4+}{}_3O_7$ - $R^{3+}{}_2R^{4+}{}_2O_7$, suggests that the Ti^{3+}-content is up to 18% of the total Ti. HAGGERTY (1978) reported a similar Ti^{3+}-content in phase T in an Allende inclusion. Figures 9a and b are plots of R^{2+} *versus* R^{3+} and R^{4+}, respectively. Most of the data are plotted on a tie line between the stoichiometric $R^{2+}R^{4+}{}_3O_7$ and $R^{3+}{}_2R^{4+}{}_2O_7$, indicative of a solid solution between them. Only a few plots show a deviation to the right side of the line, probably due to contamination of the coexisting armalcolites. Besides Ti^{3+}, phase T also contains significant amounts of other trivalent cations, including Cr_2O_3 (0.71–6.39%) and Al_2O_3 (0.24–3.90%). Figure 10 demonstrates a large variation in the divalent cations in phase T, ranging from Ca-rich to Mg, Fe-rich. Plots of phase T below the line of $R^{2+}R^{4+}{}_3O_7$ are due to presence of $R^{3+}{}_2R^{4+}{}_2O_7$. Phase T also contains V_2O_3 (<1.10%), ZrO_2 (<0.20%), Sc_2O_3 (<0.17%) and MnO (<0.27%).

In order to plot armalcolites on the same diagrams of Figs. 9 and 10, their atomic compositions are also normalized to an oxygen number of 7. Our analyses of

Table 5. Representative compositions of Ca-poor pyroxene (wt%).

	C#1						*W2#4*			
	1	2	3	4	5	6	7	8	9	10
SiO_2	57.1	56.5	54.4	54.1	57.5	56.6	56.1	57.2	56.7	56.8
TiO_2	1.43	2.50	3.05	3.21	0.95	1.17	0.83	0.29	0.69	0.66
Al_2O_3	2.42	2.94	4.08	3.53	2.61	4.03	2.44	1.95	2.18	1.88
Cr_2O_3	0.80	1.30	1.88	1.93	0.69	0.71	1.13	0.75	1.39	1.24
FeO	0.56	0.59	0.56	0.96	0.39	0.67	0.67	0.51	0.89	0.67
MnO	0.17	0.11	0.16	0.14	0.14	0.13	0.28	0.14	0.22	0.30
MgO	34.2	34.6	31.6	33.8	35.6	35.9	31.1	35.1	35.2	33.4
CaO	4.76	2.91	5.22	2.47	3.34	2.21	5.88	2.45	1.62	3.56
Na_2O	n.d.	0.05	0.04	n.d.	n.d.	n.d.	n.d.	n.d.	n.d.	0.04
Total	101.4	101.5	101.0	100.2	101.2	101.4	98.4	98.4	98.9	98.5
	normalized to oxygen number of 6									
Si	1.921	1.895	1.853	1.851	1.928	1.891	1.949	1.964	1.942	1.961
Ti	0.036	0.063	0.078	0.082	0.024	0.029	0.022	0.007	0.018	0.017
Al	0.096	0.116	0.164	0.142	0.103	0.159	0.100	0.079	0.088	0.077
Cr	0.021	0.034	0.051	0.052	0.018	0.019	0.031	0.020	0.038	0.034
Fe	0.016	0.017	0.016	0.027	0.011	0.019	0.020	0.015	0.026	0.019
Mn	0.005	0.003	0.005	0.004	0.004	0.004	0.008	0.004	0.006	0.009
Mg	1.716	1.732	1.604	1.723	1.779	1.790	1.613	1.799	1.799	1.716
Ca	0.172	0.105	0.190	0.090	0.120	0.079	0.219	0.090	0.060	0.132
Na	0.000	0.003	0.003	0.000	0.000	0.000	0.000	0.000	0.000	0.003
Sum	3.984	3.968	3.963	3.970	3.987	3.991	3.963	3.978	3.976	3.968
Fs	1	1	1	1	1	1	1	1	1	1
Wo	9	6	10	5	6	4	12	5	3	7
En	90	93	89	94	93	95	87	94	95	92

Note: 1) 1–4:in the host; 5–6: in pyroxene layer; 7–8: in poikilitic part; 9–10: in dendritic part.
2) n.d.- below detect limits (the same as before).

armalcolites show somewhat deviation from the stoichiometric compositions, probably due to contamination by perovskite or geikielite, the latter is commonly associated with Ca-rich armalcolite. Figures 9 and 10 also include literature data of armalcolite for comparison. The original data were recalculated before the plotting, because they deviate from the stoichiometric composition with a large deficiency in sum of the cations, suggestive of Ti^{3+}. Our recalculation suggests the presence of Ti^{3+}-component up to 24% of the total Ti in the armalcolite in CV3 chondrites. On the other hand, armalcolites in Ningqiang do not seem to contain Ti^{3+} either in the (Mg, Fe)-rich or in the Ca-rich ones. The contents of CaO, MgO, and FeO are distinctly different in the Ca-rich armalcolite (19.5–24.8, 1.76–5.05 and 0.34–1.78%, respectively) and the Mg, Fe-rich armalcolite (1.04–1.51, 16.0–18.2 and 6.14–7.09%, respectively), while the contents of Al_2O_3 (0.70–2.85%) and Cr_2O_3 (0.41–1.80%) are the same in both. V_2O_3 (<0.38%) and ZrO_2 (<0.12%) were detected in both Ca-rich and Mg, Fe-rich armalcolites.

Geikielite and perovskite in *C#1* contain significant amounts of trivalent cations, such as Cr_2O_3 (0.95–1.61, 0.96–2.98%, respectively) and Al_2O_3 (1.96–2.31, 0.37–1.20%, respectively). In addition, the deficiency of the cations in geikielite and

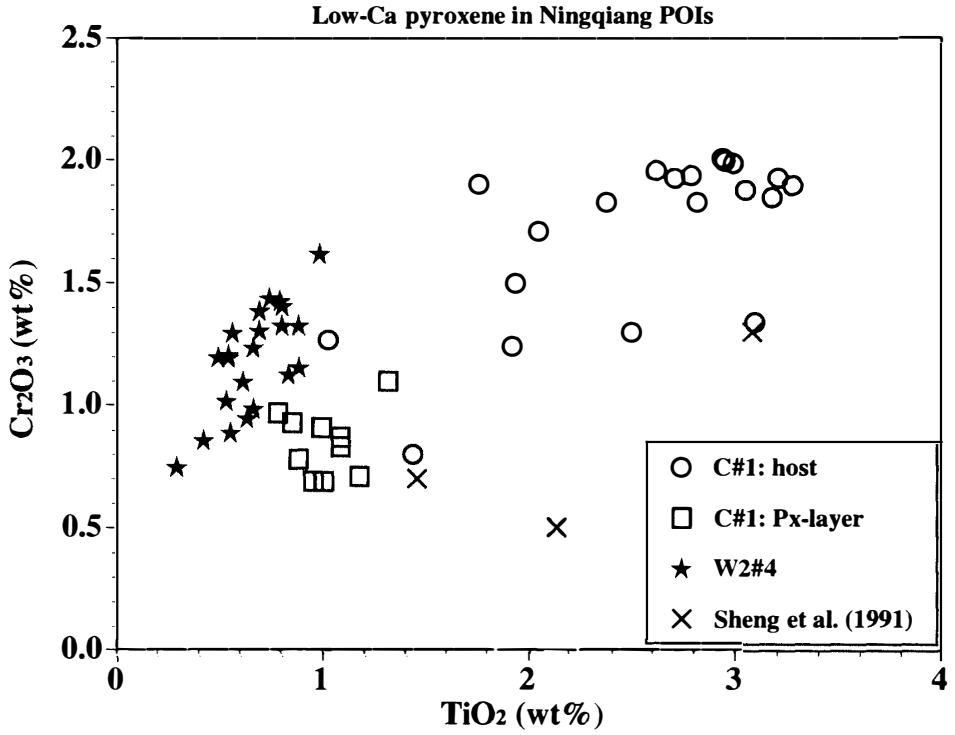

Fig. 8. TiO_2-Cr_2O_3 plot of Ca-poor pyroxene. The grains in the host in C#1 contain the highest TiO_2 and Cr_2O_3, while those in W2#4 have the lowest TiO_2-content. Abbreviation is the same as above.

perovskite (Table 6) seems to indicate the presence of Ti^{3+}. Our calculation based on the assumption of substitution of $(R^{2+}+R^{4+})-2R^{3+}$ suggests that the Ti^{3+}-content is up to 21% of total Ti in both geikielite and perovskite. However, we suspect the possibility of contamination by the coexisting armalcolites or phase T. Geikielite contains 8.25–9.76% FeO and 0.30–0.37% MnO, while perovskite is poor in these components (0.35–1.69% FeO, and MnO is below the detection limit). V_2O_3 (<0.45 wt%), ZrO_2 (<0.20%) and Sc_2O_3 (<0.08%) were detected in both of perovskite and geikielite. Only two grains of rutile were analyzed, containing 91.0% TiO_2, 3.36% Cr_2O_3, 0.68% Al_2O_3, 1.54% FeO, 1.91% CaO and 0.56% MgO (Table. 6).

Accessory phases: Fine-grained Cr-bearing phases are rarely found in the interstitial assemblages. One of them, associated with phase T, spinel, plagioclase and awaruite, contains 57.8% Cr_2O_3, 11.2% FeO, 11.2% MgO, 3.46% V_2O_3 with SiO_2, TiO_2, Al_2O_3, and NiO which could be due to the beam overlapping on the surrounding phases. Recalculation by subtracting SiO_2 (plagioclase), TiO_2 (phase T), Al_2O_3 (spinel and plagioclase) and NiO (awaruite with atomic ratio of Ni/Fe=3:1) gives a formula of $(Fe_{0.3}Mg_{0.7})(Cr_{1.88}V_{0.12})_2O_4$, suggestive of magnesian chromite. Wollastonite contains minor Al_2O_3 (0.11–0.42%), FeO (0.13–0.66%), MgO (0.09–0.31%) and Na_2O (0.18–0.27%). Hedenbergite ($Fs_{45-46}Wo_{50-51}En_4$) contains 1.45–1.48% Al_2O_3 and 1.25–1.30% MgO.

Table 6. Representative compositions of Ti-rich oxides (wt%).

	Rutile	Perovskite	Geikielite	Armalcolite	Ca-armalcolite	Phase T			
	1	2	3	4	5	6	7	8	9
SiO_2	0.81	0.29	n.d.	n.d.	0.22	0.21	0.16	0.17	0.52
TiO_2	91.0	59.9	63.2	72.9	70.7	83.3	78.1	81.2	82.8
Al_2O_3	0.68	1.20	1.97	2.85	0.70	0.55	1.79	1.73	3.20
Cr_2O_3	3.36	0.96	0.95	1.80	0.41	3.72	6.39	1.32	2.06
FeO	1.54	0.35	9.76	6.14	1.28	1.14	3.74	2.84	0.62
MnO	0.04	n.d.	0.34	0.16	0.06	0.06	0.21	0.27	0.09
MgO	0.56	1.03	23.1	16.0	3.32	0.61	7.25	11.7	4.70
CaO	1.91	34.0	0.65	1.51	21.0	10.2	1.68	0.79	5.86
Na_2O	0.03	0.41	0.07	n.d.	0.19	0.10	0.04	0.04	0.06
V_2O_3	0.11	0.45		n.d.	0.34	0.14	1.10	0.46	0.86
ZrO_2	0.07	0.11			0.12	0.13	0.04	0.08	0.19
Sc_2O_3	n.d.	0.08			n.d.	n.d.	n.d.	0.06	0.15
Total	100.1	98.8	100.1	101.4	98.4	100.2	100.4	100.7	101.0
				atomic compositions					
O	2.000	3.000	3.000	5.000	5.000	7.000	7.000	7.000	7.000
Si	0.011	0.006	0.000	0.000	0.008	0.010	0.008	0.008	0.024
Ti	0.924	1.013	0.995	1.858	1.930	3.038	2.819	2.873	2.925
Al	0.011	0.032	0.049	0.114	0.030	0.031	0.101	0.096	0.178
Cr	0.036	0.017	0.016	0.049	0.012	0.143	0.243	0.049	0.076
Fe	0.017	0.007	0.171	0.174	0.039	0.046	0.150	0.112	0.024
Mn	0.000	0.000	0.006	0.005	0.002	0.002	0.008	0.011	0.003
Mg	0.011	0.034	0.721	0.809	0.179	0.044	0.519	0.823	0.329
Ca	0.028	0.820	0.014	0.055	0.815	0.531	0.086	0.040	0.295
Na	0.001	0.018	0.003	0.000	0.014	0.009	0.003	0.003	0.005
V	0.001	0.008		0.000	0.010	0.005	0.042	0.017	0.032
Zr	0.000	0.001			0.002	0.003	0.001	0.002	0.004
Sc	0.000	0.002			0.000	0.000	0.000	0.003	0.006
Sum	1.041	1.959	1.974	3.063	3.040	3.863	3.981	4.036	3.903
$Ti^{3+}/\Sigma Ti$		0.122	0.077			0.157	0.024		0.116

Note: 1) $Ti^{3+}/\Sigma Ti$: Calculated with assumption of stoichiometries of the Ti-rich oxides.
2) n.d. - below detection limits, which are 0.02 for FeO, 0.04 for ZrO_2, and 0.01 for the others (1σ).

6. Discussion

6.1. Crystallization of the POIs

Similar to the POIs in CV3 chondrites, petrographical and mineralogical evidence suggests that Ningqiang POIs were once melted. Both *C#1* and *W2#4* are spherical in shape. *W2#4* partly shows the dendritic texture of plagioclase enclosing numerous, oriented fine-grained Ca-poor pyroxene, strongly suggestive of crystallization from a melt. The euhedral shape of the predominant plagioclase and orientation of olivine enclosed in single crystals of plagioclase in *C#1* is consistent with that they crystallized from melt. The occurrence of Ca-rich pyroxene mantling Ca-poor pyroxene in both of the inclusions is also typical of crystallization from melt. The crystallization sequences of minerals based on textural observations are spinel > olivine > plagioclase > Ca-poor

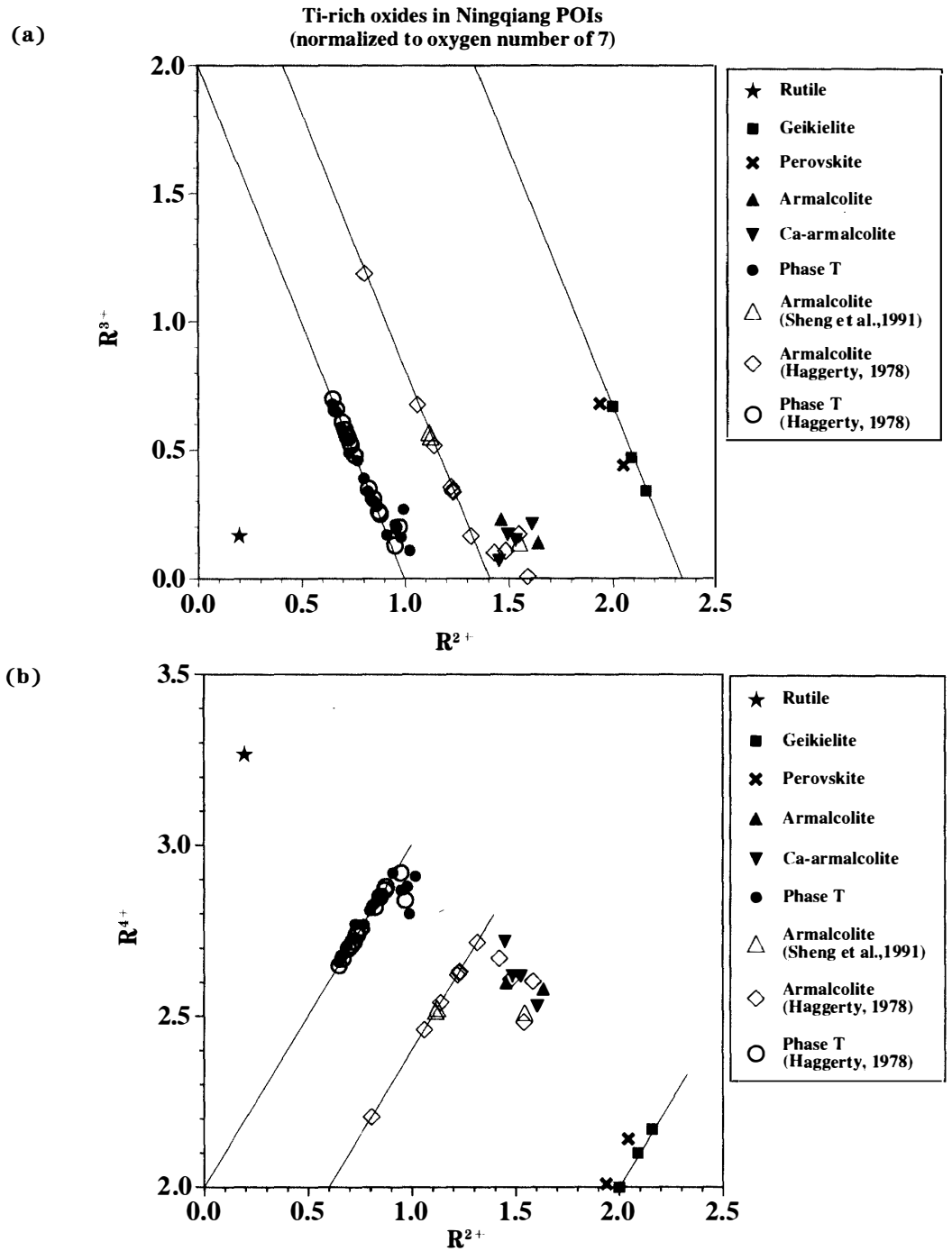

Fig. 9. Plots of R^{2+}-R^{3+} (a) and R^{2+}-R^{4+} (b) of Ti-rich oxides. Data are normalized to an oxygen number of 7 and recalculated with assumption of stoichiometries of the Ti-rich oxides. Similar to grains in Allende, data of phase T in Ningqiang are plotted on a tie line between $R^{2+}R^{4+}{}_3O_7$ and $R^{3+}{}_2R^{4+}{}_2O_7$, indicative of solid solution between these two components. Analyses of Ca-rich and Mg, Fe-rich armalcolites in Ningqiang show somewhat of a deviation from the stoichiometric line probably due to contamination from geikielite or perovskite. Compositions of perovskite and geikielite seem to be plotted on a line of substitution of $(R^{2+}+R^{4+})$-$2R^{3+}$. However, their trivalent cations such as Cr, Al and proposed Ti^{3+} may be due to contamination.

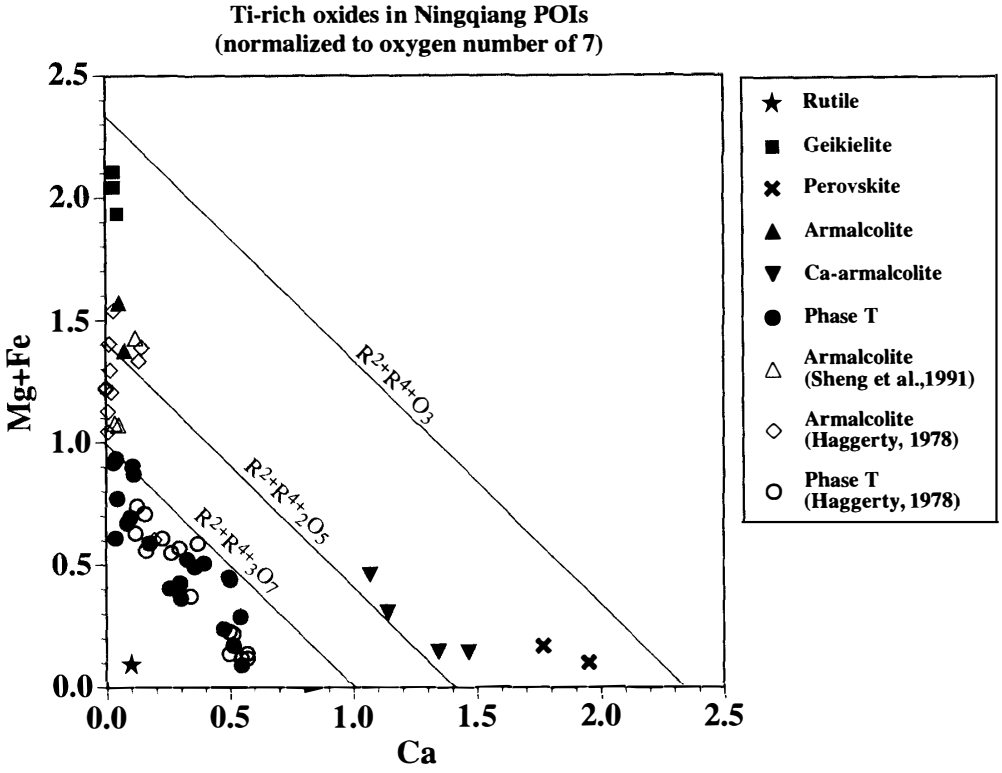

Fig. 10. Plot of Ca versus Mg+Fe, evidently distinguishing geikielite from perovskite, Ca-armalcolite from Mg, Fe-armalcolite. Phase T shows large variation in Ca, Mg and Fe content, similar to the grains in Allende. Plots of phase T below the line of $R^{2+}R^{4+}{}_3O_7$ are due to presence of $R^{3+}{}_2R^{4+}{}_2O_7$, while deviation of Ca-rich and Mg, Fe-rich armalcolites from the line of $R^{2+}R^{4+}{}_2O_5$ are probably due to contamination from geikielite or perovskite. Both geikielite and perovskite are plotted below the line of $R^{2+}R^{4+}O_3$, suggestive of presence of trivalent cations or contamination. The data are also normalized to an oxygen number of 7.

and Ca-rich pyroxenes > Ti-rich oxides in *C#1*, and spinel and olivine > plagioclase and Ca-poor pyroxene > Ca-rich pyroxene > Ti-rich oxides in *W2#4*. These sequences are inconsistent with a classical condensation sequence in which Ca-rich pyroxene is followed by plagioclase and Ca-poor pyroxene (YONEDA and GROSSMAN, 1995).

Figure 11 shows the bulk compositions of *C#1* and *W2#4* on An-Fo-SiO_2 diagram. *C#1* plots in the spinel field (Sp+L), hence spinel is the first phase to precipitate. In the case of equilibrium, spinel is expected to be exhausted before the residual melt moves away from point D, however, spinel is abundant in *C#1*. It is likely that the droplet cooled fast and hence spinel was isolated in plagioclase and olivine. Following crystallization of spinel, olivine and plagioclase crystallize. Later, pyroxene begins to crystallize at point R. This sequence is consistent with the observation of textural relationship in *C#1*. In the case of *W2#4*, spinel, plagioclase and olivine should crystallize first, followed by pyroxene. This mineral assemblage of anorthite, pyroxene and olivine is observed in the poikilitic part. The residual melt will continuously move away from point R in case of disequilibrium, and crystallize anorthite together with pyroxene, as observed in the dendritic part of the inclusion. In both *C#1* and

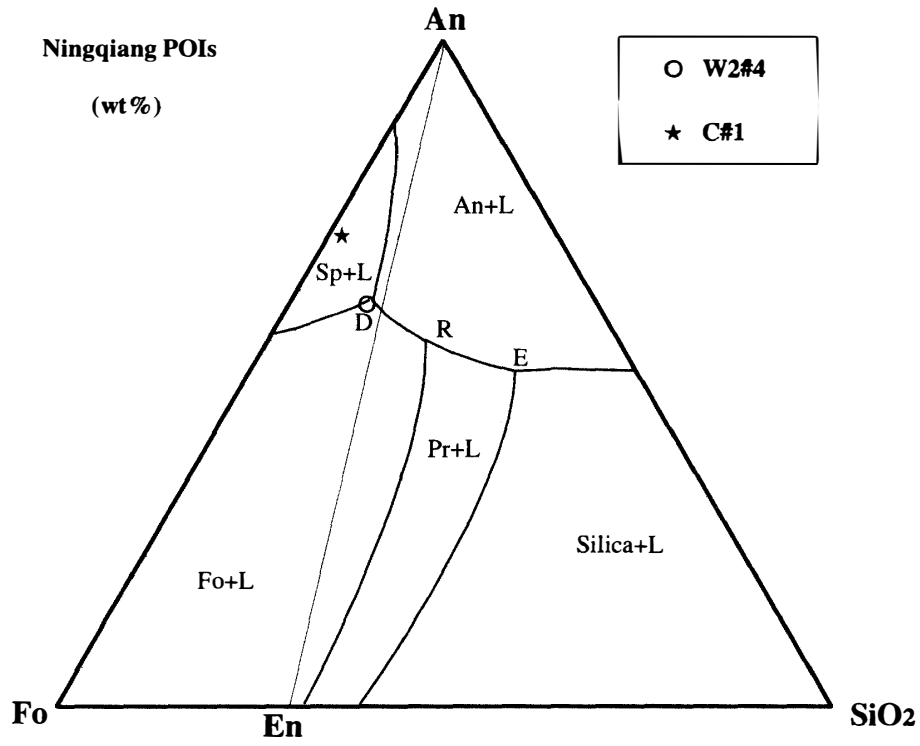

Fig. 11. Bulk compositions of C#1 and W2#4 plotted on An-Fo-SiO_2 diagram. C#1 plots in the spinel field (Sp+L), hence the expected crystallization sequence is spinel > olivine and plagioclase > pyroxene, and is consistent with the observation. The spinel has not been exhausted, probably due to rapid cooling during the crystallization. In the case of W2#4, spinel, plagioclase and olivine should crystallize first, followed by pyroxene, being consistent with the observation in the poikilitic part. The residual melt will continuously move away from point R in case of disequilibrium, and crystallize anorthite together with pyroxene as observed in the dendritic part. Abbreviations: anorthite (An), forsterite (Fo), enstatite (En), protoenstatite (Pr), and liquid (L).

W2#4, the interstitial assemblages crystallized from the last residual melts which were enriched in TiO_2 and Cr_2O_3.

Compositions of the coexisting Ca-rich and Ca-poor pyroxenes in both *C#1* and *W2#4* were used to calculate closure temperature of the pyroxene pair on the basis of a two-pyroxene thermometer (LINDSLEY and ANDERSEN, 1983). The calculated temperatures range from 1200°C to higher than 1300°C using the compositions of Ca-rich pyroxenes, or from 1200°C to 1300°C using those of Ca-poor pyroxenes in both POIs. Such high closure temperatures suggest fast cooling of both inclusions after crystallization.

Although it is possible for spinel to crystallize from a melt with a bulk composition of *C#1*, the chemical composition of the spinel is in conflict with such an origin. The high content and normal zoning of Cr_2O_3 are expected for spinel crystallizing from a Cr_2O_3-bearing melt since Cr_2O_3 strongly prefers spinel. SHENG *et al.* (1991) reported Cr partition coefficient of ~40 between spinel and a melt with the bulk composition of POIs. This means that spinel crystallizing from a melt with bulk compositions of *C#1* (0.76% Cr_2O_3) will contains ~30% Cr_2O_3. In contrast, spinel enclosed

in plagioclase and olivine in *C#1* are Cr_2O_3-poor. Furthermore, spinels in the spinel-olivine-rich zone are reversely zoned with a thin Cr_2O_3-rich rim, instead of normal zoning predicted for crystallization. The Cr_2O_3-content of spinel in *W2#4* is also much lower than that expected for equilibrium crystallization. Thus, we propose that most spinels in both *C#1* and *W2#4* are relict grains.

From the texture, the pyroxene layer appears to have crystallized from a melt. There are two possibilities for the formation of the pyroxene layer: 1) it formed from the same melt as the host, and 2) it formed by melting of accretionary rim on the host. The first possibility cannot be easily explained since only pyroxenes crystallized in this layer. The second possibility has the difficulty that a precursor material consisting only of pyroxenes is unlikely. Formation of the pyroxene layer is, therefore, not yet understood.

6.2. *Formation of Ti-rich oxide assemblages*

Distribution of titanium in refractory inclusions seems to be related to petrographic type. The major Ti-carrier phases are perovskite and partly hibonite in Type A inclusions, fassaite in Types B and C inclusions, and phase T, armalcolite and fassaite in the POIs. The variety of these Ti-carrier phases is not related to the bulk TiO_2-contents, because the bulk TiO_2 is not significantly different among these petrographic types (BECKETT and STOLPER, 1994; SHENG *et al.*, 1991; WARK, 1987; WARK and LOVERING, 1982).

C#1 contains ~2.3% TiO_2 in bulk composition, significantly higher than those of *W2#4* (0.6%) and most of the POIs in other chondrites (0.1–1.8%, SHENG *et al.*, 1991). This may explain the high abundance of Ti-rich oxides in *C#1*. However, occurrence of the Ti-rich oxides in the low-Ti *W2#4* suggests that the bulk TiO_2-content is not always a key factor in determining the formation of these phases. A more significant factor is whether the other Ti-carrier phases crystallized or not. For example, fassaite consumes almost all TiO_2 in the residual melt during its crystallization in Types B and C inclusions. On the other hand, POIs contain only a small amount of Ca-rich pyroxene usually with low TiO_2-content. In the case of *C#1*, crystallization of plagioclase and olivine critically increases the concentration of TiO_2 in the residual melt from ~2.3% to ~8.6% (by simply moving out plagioclase and olivine), which is higher than the TiO_2-content of the Ca-rich pyroxene (Fig. 7). Hence, late crystallization of the relatively low-TiO_2 Ca-rich and Ca-poor pyroxenes will also increase the concentration of TiO_2 in the residual melt. The high TiO_2/Al_2O_3 ratio of the Ca-rich pyroxene and the presence of some TiO_2-bearing spinels in the center of *C#1* may reflect the high TiO_2-enrichment of the residual melt. The concentration of CaO in the residual melt hardly changes from 12.1% to 11.7% after all of plagioclase, olivine and spinel crystallize. The ratio of TiO_2/CaO will increase as the residual melt becomes enriched in TiO_2. The high ratio of TiO_2/CaO may explain the crystallization of abundant phase T and armalcolite in comparison with rare perovskite.

7. Summary

(1) The Ningqiang POIs are texturally and mineralogically similar to the POIs in

CV3 chondrites. Their petrographical and mineralogical characteristics suggest that the POIs crystallized from melts, and the high closure temperature of their pyroxenes suggests fast cooling after crystallization.

(2) The Ningqiang POIs are characterized by the interstitial assemblages consisting of Ca-rich and Ca-poor pyroxenes, Ti-rich oxides and the other phases. This is the first report of Ca-rich armalcolite (19.5–24.8% CaO) and geikielite, and second report of phase T in meteorites. The composition of phase T varies from Ca-rich to Mg, Fe-rich, and shows significant presence of Ti^{3+}, up to 18% of the total Ti.

(3) Ti-rich oxides are the last phases to crystallize in the POIs. Precipitation of these Ti-rich oxides may be related to the low abundance of Ca-rich pyroxene.

Acknowledgments

We are very grateful to Dr. A. E. RUBIN for kindly loaning us the inclusion *C#1*, to Dr. M. K. WEISBERG and Dr. T. FUJITA for their constructive reviews. This work is supported by the Japan Society for Promotion of Sciences.

References

BECKETT, J. R. and STOLPER, E. (1994): The stability of hibonite, melilite and other aluminous phases in silicate melts: Implications for the origin of hibonite-bearing inclusions from carbonaceous chondrites. Meteoritics, **29**, 41–65.

BENCE, A. E. and ALBEE, A. L. (1968): Empirical correction factors for the electron microanalysis of silicates and oxides. J. Geol., **76**, 382–403.

EL GORESY, A., PALME, H., YABUKI, H., NAGEL, K., HERRWERTH, I. and RAMDOHR, P. (1984): A calcium-aluminum-rich inclusion from the Essebi (CM2) chondrite: Evidence for captured spinel-hibonite spherules and for an ultra-refractory rimming sequence. Geochim. Cosmochim. Acta, **48**, 2283–2298.

HAGGERTY, S. E. (1978): The Allende meteorite: Solid solution characteristics and the significance of a new titanate mineral series in association with armalcolite. Proc. Lunar Planet. Sci. Conf., 9th, 1331–1344.

KALLEMEYN, G. W. (1996): The classificational wanderings of the Ningqiang chondrite. Lunar and Planetary Science XXVII. Houston, Lunar Planet. Inst., 635–636.

KALLEMEYN, G. W., RUBIN, A. E. and WASSON, J. T. (1991): The compositional classification of chondrites: V. The Karoonda (CK) group of carbonaceous chondrites. Geochim. Cosmochim. Acta, **55**, 881–892.

KIMURA, M., NOGUCHI, T., LIN, Y. and WANG, D. (1997): Petrology and mineralogy of an unusual Ningqiang carbonaceous chondrite. Geochemical Studies on Synthetic and Natural Rock Systems, ed. by A. K. GUPTA *et al.* New Delhi, Allied Publ., 153–165.

LIN, Y. and KIMURA, M. (1996a): A new kind of plagioclase-rich inclusions in the Ningqiang carbonaceous chondrite. Lunar and Planetary Science XXVII. Houston, Lunar Planet. Inst., 755–756.

LIN, Y. and KIMURA, M. (1996b): Discovery of complex titanium oxide associations in a plagioclase-olivine inclusions (POI) in the Ningqiang carbonaceous chondrite. Lunar and Planetary Science XXVII. Houston, Lunar Planet. Inst., 753–754.

LIN, Y., KIMURA, M. and WANG, D. (1996): Refractory inclusions in the Ningqiang carbonaceous chondrite. Antarctic Meteorites XXI. Tokyo, Natl Inst. Polar Res., 87–89.

LINDSLEY, D. H. and ANDERSEN, D. J. (1983): A two-pyroxene thermometer. Proc. Lunar Planet. Sci. Conf., 13th, Pt. 2, A887–A906 (J. Geophys. Res., **88** Suppl.).

RUBIN, A. E., WANG, D., KALLEMEYN, G. W. and WASSON, J. T. (1988): The Ningqiang meteorite: Classification and petrology of an anomalous CV chondrite. Meteoritics, **23**, 13–23.

SHENG, Y. J., HUTCHEON, I. D. and WASSERBURG, G. J. (1991): Origin of plagioclase-olivine inclusions in carbonaceous chondrites. Geochim. Cosmochim. Acta, **55**, 581–599.

WARK, D. A. (1987): Plagioclase-rich inclusions in carbonaceous chondrite meteorites: Liquid condensates? Geochim. Cosmochim. Acta, **51**, 221–242.

WARK, D. A. and LOVERING, J. F. (1982): The nature and origin of type B1 and B2 Ca-Al-rich inclusions in the Allende meteorite. Geochim. Cosmochim. Acta, **46**, 2581–2594.

WEISBERG, M. K., PRINZ, M., ZOLENSKY, M. E., CLAYTON, R. N., MAYEDA, T. K. and EBIHARA, M. (1996): Ningqiang and its relationship to oxidized CV3 chondrites. Meteorit. Planet. Sci., **31**, Suppl., A150–A151.

YONEDA, S. and GROSSMAN, L. (1995): Condensation of CaO-MgO-Al_2O_3-SiO_2 liquids from cosmic gases. Geochim. Cosmochim. Acta, **59**, 3413–3444.

(Received September 30, 1996; Revised manuscript accepted Novmber 27, 1996)